

Low-lying resonances in electron-neon scattering: Measurements at 4-meV resolution and comparison with theory

J. Bömmels,¹ K. Franz,¹ T. H. Hoffmann,¹ A. Gopalan,¹ O. Zatsarinny,² K. Bartschat,² M.-W. Ruf,¹ and H. Hotop¹

¹*Fachbereich Physik, Technische Universität Kaiserslautern, D-67653 Kaiserslautern, Germany*

²*Department of Physics and Astronomy, Drake University, Des Moines, Iowa 50311, USA*

(Received 6 August 2004; published 6 January 2005)

An electron scattering apparatus, combining a laser photoelectron source, a triply differentially pumped supersonic beam target, and several electron multipliers for simultaneous detection of elastically scattered electrons and of metastable atoms due to inelastic scattering, has been used for an improved study of electron-neon scattering over the energy range 16–19 eV at experimental energy widths of 4–6 meV. Accurate values for the energies and widths of the low-lying $\text{Ne}^-(2p^5 3s^2 \ ^2P_{3/2,1/2})$ Feshbach resonances have been determined from detailed analyses of the resonance profiles (measured at the five scattering angles 22.5°, 45°, 90°, 112.5°, 135°). In addition, the excitation function for the production of metastable $\text{Ne}^*(2p^5 3s \ ^3P_{2,0})$ atoms has been measured from threshold to 19 eV; from a fit to its onset, the absolute electron energy scale is established to better than 0.5 meV. While our resonance widths agree with the recommended values, the resonance energies differ by an amount larger than the quoted respective uncertainties. The experimental data are also compared with theoretical results, calculated with an improved *R*-matrix approach. Very good overall agreement between the experimental and the theoretical results is observed. A very sharp Feshbach resonance, associated with the $\text{Ne}^*(2p^5 3p[5/2]_2)$ level, has been theoretically predicted and experimentally confirmed at 18.527 eV.

DOI: 10.1103/PhysRevA.71.012704

PACS number(s): 34.80.Bm, 34.80.Dp, 31.25.Jf, 32.70.Jz

I. INTRODUCTION

Collisions of low-energy electrons with atoms, molecules, and ions are important elementary processes in technical and natural plasmas including gaseous discharges, flames, laser plasmas, high-current switches, arcs, and stellar atmospheres. These processes have been investigated for about 100 years, but most notably since the 1960s with the availability of improved vacuum and detector technologies and following the discovery of narrow resonances in electron scattering from atoms and molecules [1–9]. Using conventional equipment for electron-energy selection (e.g., spherical or cylindrical electrostatic condensers), typical energy widths in low-energy electron scattering experiments involving gaseous targets have been in the range 20 to 60 meV full width half maximum (FWHM). In a few cases, energy widths down to about 8 meV (FWHM) have been obtained [9–14].

As a promising alternative to reach very high resolution, near-threshold photoionization of atoms has been exploited as a source for monoenergetic electrons. This approach has been applied in several experiments to study anion formation due to low-energy electron attachment [9,15] as well as total [16–19] and angle-differential [16,17,20–22] electron scattering cross sections. In a pioneering experiment, Gallagher and co-workers used photoionization of metastable $\text{Ba}^*(^1D_2)$ atoms by a cw He-Cd laser at 325 nm to create electron beams with up to 10 pA of current and to study elastic scattering from He and Ar atoms as well as from N_2 molecules [20,21]. Effective linewidths of 5–6 meV were observed for the narrow Feshbach resonances in Ar at 11.1 eV and N_2 at 11.48 eV [20], for which the estimated natural widths are about 3 meV [5,23] and 0.6 meV [24], respectively. More recently, Gopalan *et al.* [22] combined a laser photoelectron source with a triply differentially pumped supersonic beam,

thus achieving a well-collimated target whose density exceeded the background density by a factor of 100–200. In a first application they restudied the $\text{He}^-(1s2s^2)$ resonance at energy widths around 7.5 meV. In the present work, we extend these measurements to Ne atoms; energy widths down to 4 meV have been achieved at satisfactory signal to background ratios. Elastic electron scattering spectra in the region of the low-lying Feshbach resonances $\text{Ne}^-(2p^5 3s^2 \ ^2P_{3/2,1/2})$ are reported for five angles (22°, 45°, 90°, 112°, and 135°) and consistently analyzed, thus yielding accurate values for the respective resonance widths and resonance energies. The latter are referenced to the onset for the production of the lowest metastable level $\text{Ne}^*(3s \ ^3P_2)$, respectively, which was measured simultaneously with the elastic scattering. In Sec. II we summarize the theoretical formulas needed for the analysis of the experimental data and briefly outline the semirelativistic B-spline *R*-matrix approach used in the numerical calculations. In Sec. III we describe the experimental apparatus and some test measurements. In Sec. IV we report the experimental results and the analysis of the resonance profiles; moreover, we present a comparison with the *R*-matrix calculations. We conclude with a brief summary and some perspectives.

II. THEORETICAL DESCRIPTION

A. Partial wave analysis of the angle-dependent $\text{Ne}^-(2p^5 3s^2 \ ^2P_{3/2,1/2})$ resonance profiles

The differential cross section $d\sigma/d\Omega$ for elastic potential electron scattering in the presence of significant spin-orbit coupling is given by [25,26]

$$\frac{d\sigma}{d\Omega}(\theta, E) = |f(\theta, E)|^2 + |g(\theta, E)|^2, \quad (1)$$

where the direct and exchange amplitudes f and g are given by partial wave sums as follows:

$$f(\theta, E) = \frac{1}{2ik} \sum_{L=0}^{\infty} \{ (L+1) [\exp(2i\delta_L^+(E)) - 1] + L [\exp(2i\delta_L^-(E)) - 1] \} P_L(\cos \theta), \quad (2)$$

$$g(\theta, E) = \frac{1}{2ik} \sum_{L=0}^{\infty} \{ \exp(2i\delta_L^+(E)) - \exp(2i\delta_L^-(E)) \} P_L^1(\cos \theta). \quad (3)$$

Here, k is the linear momentum of the electron, and the functions $P_L(\cos \theta)$ are the standard Legendre polynomials while $P_L^1(\cos \theta)$ ($L \geq 1$) denotes an associated Legendre polynomial. Furthermore, δ_L^+ and δ_L^- represent the phase shifts in the partial wave with orbital angular momenta $L \geq 1$ and total electronic angular momenta $J^+ = L + \frac{1}{2}$ and $J^- = L - \frac{1}{2}$. In the absence of spin-orbit interaction (as well as for $L=0$), $\delta_L^+ = \delta_L^- = \delta_L$ and $g(\theta, E) = 0$. In the energy range of the spin-orbit split $\text{Ne}^-(2p^5 3s^2 {}^2P_{3/2,1/2})$ Feshbach resonances (with an energy separation close to that of the $2p^5$ core, i.e., close to 0.1 eV) the phase shifts δ_L^+ and δ_L^- for the partial wave $L=1$ attain different values due to the additional influence of the respective resonance phase shifts δ_r^+ and δ_r^- ; they are introduced by the expression [25]

$$\delta_r^\pm = -\arccot[2(E - E_r^\pm)/\Gamma^\pm], \quad (4)$$

where the plus and minus sign denote the ${}^2P_{3/2}$ and ${}^2P_{1/2}$ resonance, respectively. The resonant phase shift $\delta_r^\pm(E)$ rises from 0 to π when the electron energy increases from lower to higher energies through the respective resonance energy E_r^\pm ; the breadth of the resonance region is characterized by the resonance width Γ^\pm .

For elastic electron scattering from neon atoms at energies around the $\text{Ne}^-(3s^2 {}^2P_{3/2,1/2})$ resonances (16.1–16.2 eV) [5], partial waves higher than $L_c=2$ do not penetrate significantly to the inner part of the atom (see, e.g., [27–29]) and hence predominantly feel the long-range part of the electron-atom interaction, described by the dipole polarization potential $V_{pol} = -\alpha(2r^4)^{-1}$ (α is atomic polarizability, $\alpha(\text{Ne}) = 2.6696a_0^3$ [30], a_0 is Bohr radius). Thus, for $L > L_c=2$, the phase shifts δ_L^+ and δ_L^- are very similar and, as shown by Thompson [31], the contribution to the scattering amplitude due to partial waves $L > L_c$ is well represented by the expression

$$f_B(L > L_c) = \left(\frac{\pi a k}{a_0} \right) \left[\frac{1}{3} - \frac{1}{2} \sin\left(\frac{\theta}{2}\right) - \sum_{n=1}^{L_c} \frac{P_n(\cos \theta)}{(2n+3)(2n-1)} \right]. \quad (5)$$

Using Eqs. (1)–(5) and appropriate (energy independent) background phase shifts (see Sec. IV B), differential cross

sections were evaluated and fitted to the measured resonance profiles, using Γ^\pm and E_r^\pm as adjustable parameters. The calculated differential cross sections were convoluted with a Gaussian function of adjustable width in order to simulate the energy resolution function of the experiment.

B. Numerical calculations

The numerical calculations performed for the present work are based upon the semirelativistic B-spline R -matrix (BSRM) approach described by Zatsarinny and Bartschat [32]. Since all the details of this particular method and references to earlier work, particularly to that of Zeman and Bartschat [33] using the Belfast R -matrix code [34], can be found in the above paper, only a brief summary will be given here.

The lowest 31 physical states of Ne, together with five short-range pseudostates, were included in a close-coupling-type trial function for e -Ne collisions. The latter pseudostates were specially constructed to improve the nonresonant background phase shifts in the purely elastic regime. These background phase shifts are essentially determined by the dipole polarizability of the ground state. For noble gases, this polarizability is not properly described by only a few low-lying physical states in the close-coupling expansion. Instead, significant contributions come from high Rydberg states and, even more important, from coupling to the ionization continuum.

A very important aspect of the BSRM approach, which distinguishes it substantially from nearly all other methods commonly used to describe electron collisions with atoms and molecules, is the possibility of using a set of term-dependent nonorthogonal one-electron orbitals in the multi-configuration description of the N -electron target states. For reasons of numerical convenience and stability, these orbitals, as well as the basis of continuum orbitals used to describe the projectile electron inside the R -matrix box (essentially the region where the problem is most complicated due to the highly correlated motion of $N+1$ electrons), are expanded in a numerically complete set of B-splines. Since the term dependence can be accounted for in individual members of a given target configuration, it is possible to obtain a very satisfactory description of both the energy levels and the oscillator strengths with rather small configuration-interaction expansions (see Tables 1 and 2 of [32]). In the traditional methods with an orthogonal set of one-electron orbitals, a similar accuracy can, in principle, be achieved by very large expansions using so-called pseudo-orbitals, as is done in the R -matrix with pseudostates (RMPS) method [35–37]. Very recently, results from such a calculation were reported [38], emphasizing the intermediate-energy regime where coupling to the continuum is very important. Even with hundreds of coupled states included in the close-coupling plus correlation expansion, however, the near-threshold resonance features of interest for the current work would likely not be described as well as they are in the calculations reported here [39].

Finally, it is appropriate to comment on the comparison between the experimental and theoretical energy scales. In

order to allow for a direct comparison between experiment and theory in the present work, we adjusted the theoretical N -electron target state energies before diagonalizing the $(N+1)$ -electron Hamiltonian for the collision system. This was done by ensuring the correct binding energies of all 31 physical states included in the close-coupling expansion. Looking at Table 1 of [32], typical adjustments required were about 20 meV.

III. EXPERIMENTAL APPARATUS AND PROCEDURE

The newly developed electron scattering apparatus has been described in detail in a recent paper [22]. Following the approach of Gallagher *et al.* [20,21] and Field *et al.* [17], the basic idea for achieving high energy resolution is the combination of a (laser) photoelectron source with a collimated supersonic beam target, yielding a low *a priori* energy spread in the electron beam and negligible Doppler broadening. In our work on the $\text{He}^-(1s2s^2)$ resonance [22] the demonstrated energy width (FWHM) was around 7.5 meV. In the present work on neon, several extended data runs were performed at resolutions between 4 and 6 meV.

A. Vacuum system, target beam

The apparatus consists of several separately pumped chambers. The nozzle chamber, the intermediate chamber, and the dump chamber serve to create an intense, well collimated Campargue-type [40] supersonic beam target of atoms or molecules in the reaction volume, located in the main chamber about 160 mm from the nozzle [41]. A sonic nozzle (diameter 0.2 mm) in conjunction with a conical skimmer (Beam Dynamics, Mod. 31.8, diameter 0.7 mm, Fig. 8(a) in [41]) in the nozzle chamber and a conical skimmer (diameter 1.93 mm) at the end of the intermediate chamber produce a well-collimated beam whose diameter amounts to 4.3 mm in the scattering region. At a stagnation pressure $p_0=2$ bar (nozzle temperature $T_0=300$ K) the neon target density amounts to about $2 \times 10^{12} \text{ cm}^{-3}$, as estimated from *in situ* electron impact ionization and from the pressure rise in the dump chamber [41]. Under these conditions the background neon density (due to backstreaming from the dump chamber, intrabeam scattering and scattering from the two skimmers) is at least 100 times lower. The base pressure in the main chamber (target beam off) was around 5×10^{-8} mbar in most measurements. To reduce the operating cost, the neon gas was recycled [42] during most of the measurements.

B. Laser photoelectron source, electron beam formation and product detection

The photoelectron production is based on resonant two-step photoionization of potassium atoms in a well-collimated beam (diameter 2 mm, atomic density around 10^8 cm^{-3}) [9,43–45]. The potassium beam is generated in a differentially pumped two-stage oven, operated in the effusive regime [22]. Both hyperfine components of ground state $^{39}\text{K}(4s, F=1, 2)$ atoms in the collimated beam are transversely excited to the $^{39}\text{K}^*(4p_{3/2}, F=2, 3)$ states by the first sidebands of the electro-optically modulated (frequency

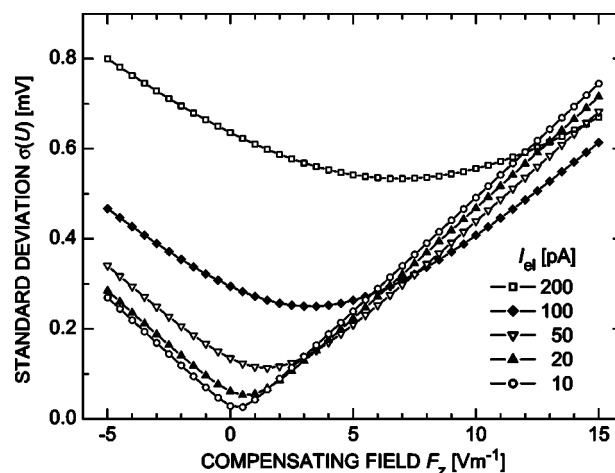


FIG. 1. Results of Monte Carlo simulations for the standard deviation $\sigma(U)$ of the potential distribution $f(U)$ in the electron source volume due to the photoion space charge and the superimposed compensation field F_z along the potassium beam for different values of the photoelectron current I_{el} and of the compensation field F_z .

220.35 MHz) output of a single-mode cw titanium:sapphire laser ($\lambda_1=766.7$ nm); the latter is long-term stabilized to the atomic transition by crossover saturation spectroscopy in an auxiliary potassium vapor cell [45]. Part of the excited state population is photoionized by interaction with the focused intracavity field of a multimode tunable dye laser (energy width 0.05 meV, power up to 7 W), operated in the blue spectral region (dye Stilbene 3). The laser diameter is about $120 \mu\text{m}$ in the 2 mm long photoionization region. Electrons are created very close to threshold ($\lambda_2=455.3$ nm, nominal energy below 0.1 meV) in a nearly homogeneous extraction field of typically 10 V m^{-1} . As confirmed by test measurements the quoted extraction field leads to an associated energy width around 1 meV in agreement with the width expected from the (calculated) laser diameter. The infrared laser (typical power around 80 mW) is superimposed collinearly with the ionization laser, entering through the terminating mirror [transmission 0.94(1)% at 455 nm and about 98% at 767 nm] of the blue laser. The infrared laser is thus also brought to a spherical focus with a diameter somewhat wider than that of the ionization laser. Test experiments showed that the photoelectron current was independent of the infrared laser power at levels above 10 mW. Typical photoelectron currents in the present measurements were in the range 50–90 pA.

In order to characterize the influence of the photoion-induced space charge on the effective energy width of the electron beam, Monte Carlo simulations were carried out in a way described previously [46]. In Fig. 1 we present the current-dependent standard deviations of the potential distribution in the electron source volume (cylinder with $120 \mu\text{m}$ diameter due to the spherical focus of the ionizing laser and 2 mm length due to the K beam diameter) which are due to the effects of photoion space charge and additional homogeneous electric fields F_z applied along the direction of the potassium beam. As seen from the results in Fig. 1, this field F_z allows us to minimize the potential variation in the elec-

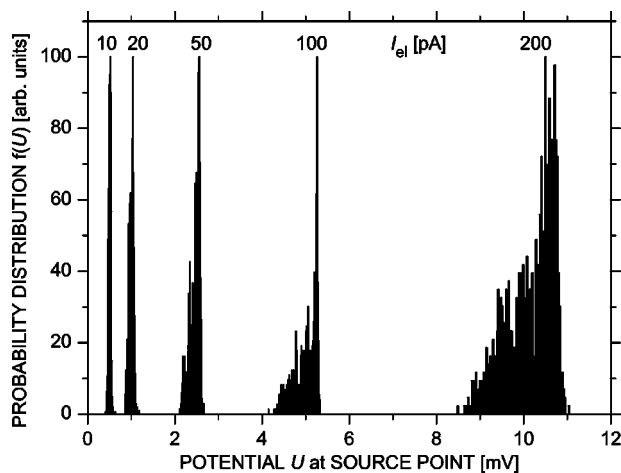


FIG. 2. Results of Monte Carlo simulations for the potential distributions $f(U)$ in the electron source volume with optimized compensation field F_z .

tron source volume which is associated with the rise of the photoion space charge potential along the vertical z direction. This possibility has been previously exploited by our group in electron attachment studies involving the potassium photoelectron source [46] and in the helium scattering experiments in which a cylindrically focused ionization laser was used [22]. Figure 2 shows the potential distributions in the photoelectron source volume which are obtained for currents in the range 10 to 200 pA when an optimized field F_z has been applied. Under these conditions we expect that at electron currents up to 100 pA the space charge related energy broadening (FWHM ≈ 2.4 standard deviations) should stay below 2 meV.

The photoelectrons are accelerated by a weak electric field (typically about 10 V m^{-1} , see above) and brought to the energy of interest by an electron optical system (see Fig. 3) which focuses the electron beam onto the perpendicular target beam. Geometric and electron optical considerations (including the divergence of the target beam, half angle 0.015 rad) indicate that the deviations from perpendicular impact are at most $\pm 0.03 \text{ rad}$, leading to negligible Doppler-type energy broadening (see below).

Five electron detectors, each equipped with a retarding electric field and a channel electron multiplier (Sjuts, Mod. KBL 10 RS, diameter of entrance cone 10 mm), serve to measure simultaneously the intensity of elastically scattered electrons at the fixed scattering angles $\theta = 22.5^\circ, 45^\circ, 90^\circ, 112.5^\circ$, and 135° (in Fig. 3 only the detector positioned at 90° with respect to the electron beam is shown). A rectangular entrance aperture (4 mm wide, 6 mm high, located 32.5 mm from the scattering center) limits the angular acceptance range of the electron detectors to $\pm 3.5^\circ$. It is followed by a circular lens element (diameter 10.6 mm , length 4 mm) and a pair of grids (diameter 10.6 mm) which form the retarding field, rejecting inelastically scattered electrons. We note that because of the well-defined scattering region and missing lenses in the detectors, electrons from all volume elements of the scattering region are expected to view the detectors with equal detection solid angles.

An additional electron multiplier (Sjuts, Mod. KBL 20 RS, diameter of entrance cone 20 mm), mounted at the kin-

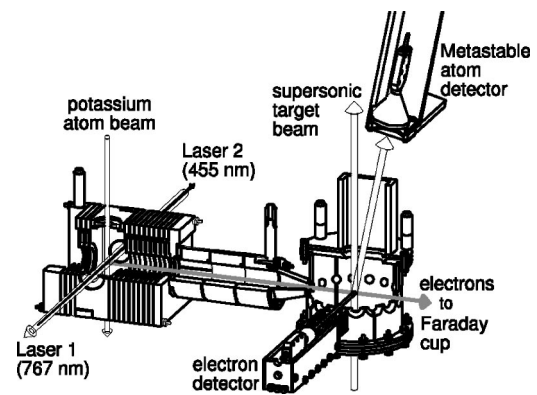


FIG. 3. Semischematic side view of the essential parts of the experimental apparatus: laser photoelectron source, electron optics, scattering chamber, and particle detectors. Only one of the five electron detectors ($\theta = 90^\circ$) is shown. In this graph, the metastable atom detector is placed in a position appropriate for the detection of metastable $\text{He}^*(2^3S_1)$ atoms, excited near threshold. For the detection of metastable Ne^* atoms, it is mounted closer to the axis of the supersonic target beam.

matically appropriate position, samples long-lived excited (“metastable”) $\text{Ne}^*(2p^5 3s^3 P_2, ^3P_0)$ atoms due to inelastic electron scattering. Ground state neon atoms (flow velocity $u = [5k_B T_0 / (2m_{\text{Ne}})]^{1/2} = 790 \text{ ms}^{-1}$ at $T_0 = 300 \text{ K}$), which are excited to the metastable $\text{Ne}^*(3s^3 P_2)$ level by a perpendicular monoenergetic electron beam at threshold (transition energy $E(^3P_2) = 16.619\,075(6) \text{ eV}$, taken from [47,48] with the conversion $1.239\,841\,857(49) \times 10^{-4} \text{ eV/cm}^{-1}$ [49]), are deflected by a (lab) angle of 4.8° . At an electron energy of 1.2 eV above threshold, for example, the deflection angles are spread over the range 3.7° to 6.2° .

C. Calibration of the absolute electron energy scale

The detection of metastable $\text{Ne}^*(3s^3 P_2)$ atoms serves an important purpose: based on the well-known threshold energy (see above) and the accurate theoretical cross section for the production of $\text{Ne}^*(3s^3 P_2)$ atoms (see below), one can precisely determine—by comparing the measured yield for metastable atom production with that obtained by convolution of the theoretical cross section with an appropriate resolution function—both the absolute electron energy scale and the effective energy width of the scattering experiment. Note that small differences exist between the laboratory electron energy $E = \frac{1}{2} m_e v_e^2$ and the relative collision energy E_{rel} in the center-of-mass frame which is given by $E_{\text{rel}} = \frac{1}{2} [m_e m_T / (m_e + m_T)] (\mathbf{v}_e - \mathbf{v}_T)^2 \approx E - (m_e / m_T) E - 2(EE_T m_e / m_T)^{1/2} \cos \alpha$ (with $\alpha = \angle(\mathbf{v}_e, \mathbf{v}_T)$ and $E_T = \frac{1}{2} m_T v_T^2 = \text{kinetic energy of target particles}$). The second term is the recoil energy E_R transferred to the target by the incoming electron while the third term represents the energy shift E_D due to the first-order Doppler effect. Near the threshold for $^{20}\text{Ne}^*(3s^3 P_2)$ excitation the recoil energy amounts to $E_R = 0.46 \text{ meV}$ and the Doppler shift to $E_D = 10.9 \text{ meV} \times \cos \alpha$, i.e., for a range of $\alpha = (\pi/2) \pm 0.03 \text{ rad}$ the Doppler shift stays below $|E_D| \leq 0.32 \text{ meV}$. When comparing the en-

ergy for the threshold of $\text{Ne}^*(3s\ ^3P_2)$ excitation with that for the position of the $\text{Ne}^-(2p\ ^3P_{3/2})$ resonance ($E \approx 16.1$ eV, $E_R = 0.44$ meV), the energy separations between the two respective electron energies in the laboratory and the center-of-mass frame differ mainly by the nonidentical recoil energies. This difference of 0.02 meV is well within the overall uncertainty of the absolute energy calibration.

As shown in Fig. 6 below, the theoretical cross section for the production of metastable $\text{Ne}^*(3s\ ^3P_2)$ atoms over the energy range from its threshold to the next onset [production of the $\text{Ne}^*(3s\ ^3P_1)$ level] is well described by the analytical function $f(E) = f_0[E - E(^3P_2)]^{0.44}$ with $f_0 = 4.3786 \times 10^{-22}$ m² and E in eV. We note that an exponent of 0.5 is expected according to Wigner's law [50] (close to threshold the outgoing inelastically scattered electron should be predominantly s wave), but in view of the high polarizability of $\text{Ne}^*(3s\ ^3P_2)$ atoms ($188a_0^3$ [30]) the Wigner law is expected to hold over only a very narrow energy range above threshold (see, e.g., [51]).

D. Voltage sources and data acquisition

The electron energy width is—in part—limited by fluctuations of the potentials applied to the various electrodes. Custom-made voltage supplies, based on 16-bit high precision digital-to-analog converters (accuracy better than 152 μ V over the full voltage range), have been built as well as a versatile graphical data acquisition system [22]. The linearity of the voltage scale has been verified by measuring the output voltage with a precise multimeter (Keithley 2700, stated resolution 10 μ V, accuracy 30 ppm). Thorough design of the electronic circuits, careful cabling (avoiding ground and shield loops) and filtering by ferrite cores ensure low noise and ripple figures in the mV range. In view of the proliferation of communication using RF waves, electromagnetic interference may influence the energy resolution.

E. Shielding of electric and magnetic fields; drifts of surface potentials

Electric stray fields in the photoionization and scattering regions were minimized by coating the metal surfaces with colloidal graphite (Kontakt Chemie, Graphit 33), sprayed on with an airbrush (see also [22] for other measures taken). Magnetic fields were shielded with a double layer of mu metal (1.5 mm thick) which reduces the residual dc magnetic field components in the chamber to values below 1 mG in the horizontal plane and well below 6 mG in the vertical direction.

A critical point in high resolution experiments are (differential) drifts in the surface potentials of the electrodes defining the average dc potentials in the electron source region and in the scattering volume. These effects appear to have influenced and partially limited the overall energy width achieved in the photoelectron scattering experiment of Gallagher *et al.* [20,21]. In the present work we diagnose these differential drifts, i.e., the variation of the potential difference U_{SP} between the scattering region and the photoelectron source volume, by measuring the variation of the energy po-

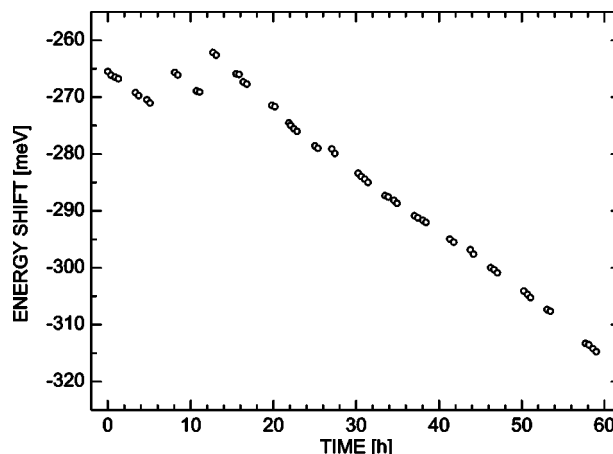


FIG. 4. Time dependence of the contact potential difference U_{SP} between the scattering region and the photoelectron source volume for the data shown in accumulated form in Fig. 7. Each circle denotes a data run over about 23 min. The typical variation amounts to $\Delta U_{SP}/\Delta t \approx -1$ meV/h.

sition of a sharp feature in the electron scattering cross section [here the energy of the $\text{Ne}^-(2p\ ^53s\ ^2P_{3/2})$ resonance] with time. The voltage U_{SP} normally is negative due to the fact that the surfaces in the photoelectron production chamber have a higher coverage with potassium than those in the scattering chamber. A potassium layer on the graphite coating generally leads to a shift in the surface potential to positive values.

In Fig. 4 we document the long-time variation of the voltage U_{SP} which—apart from opposite changes related to venting of the main chamber—exhibits a rather smooth trend with a typical slope of $\Delta U_{SP}/\Delta t \approx -1$ meV/h. Under these conditions, an overall experimental energy width of 4.0 meV (FWHM) was achieved (see below). This, to date, is the highest energy resolution realized in an angle-differential electron scattering experiment from a gaseous target.

IV. RESULTS AND DISCUSSION

A. Excitation function for the production of metastable $\text{Ne}^*(3s\ ^3P_2, ^3P_0)$ atoms

In Fig. 5 we compare the yield for the production of metastable $\text{Ne}^*(3s\ ^3P_2, ^3P_0)$ atoms, which we measured over the energy range 16–19 eV with a resolution of 5–6 meV (open circles, normalized to theory at the peak close to 16.9 eV), with the theoretical cross section, calculated with the B-spline R -matrix method. The two data sets show very good mutual agreement, especially in the shapes and energies of the various resonant structures. For energies above 17.0 eV, the theoretical cross sections are somewhat higher than the experimental data (on average by 7%). Above the onset for the formation of $\text{Ne}^*(2p\ ^53p)$ levels (18.381 62 eV [47–49]), cascade contributions, due to optical decay from the $\text{Ne}^*(2p\ ^53p)$ levels to the metastable states, start to play a role. At 19.0 eV, the cascade contribution to the metastable atom signal amounts to 38%.

We note that the excitation function for metastable Ne^* production, measured by the Manchester group [52,53] at an

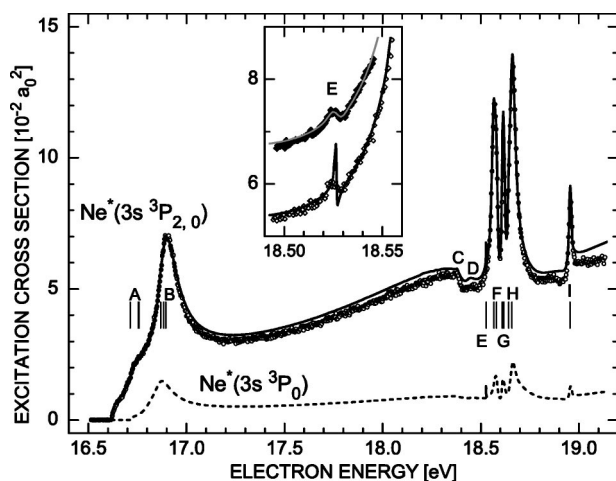


FIG. 5. Excitation cross section (in units of $10^{-2}a_0^2$, a_0 is the Bohr radius) for the production of metastable $\text{Ne}^*(3s\ ^3P_2, ^3P_0)$ atoms in the energy range 16.5 to 19.0 eV. Open circles: present measurement. Full curve: BSRM theory [including cascade contributions and assuming identical detection efficiencies for $\text{Ne}^*(3s\ ^3P_2)$ and $\text{Ne}^*(3s\ ^3P_0)$ atoms]. Broken curve: theoretical excitation function of the production of $\text{Ne}^*(3s\ ^3P_0)$ atoms, including cascade contributions. Inset: enlarged view of the data over the energy region 18.48–18.58 eV, revealing a narrow Feshbach resonance (see text).

energy width slightly below 20 meV, shows very good overall agreement with the results in Fig. 5. Due to the improved resolution, our data exhibit sharper onsets (see also Fig. 6) and somewhat narrower widths of the prominent resonances in the range 18.5–19 eV. Moreover, our data reveal the presence of a very sharp resonance at 18.527 eV with a theoretically predicted width of 0.84 meV [see inset in Fig. 5 and Table I]. The dominant component of this resonance in Ra-

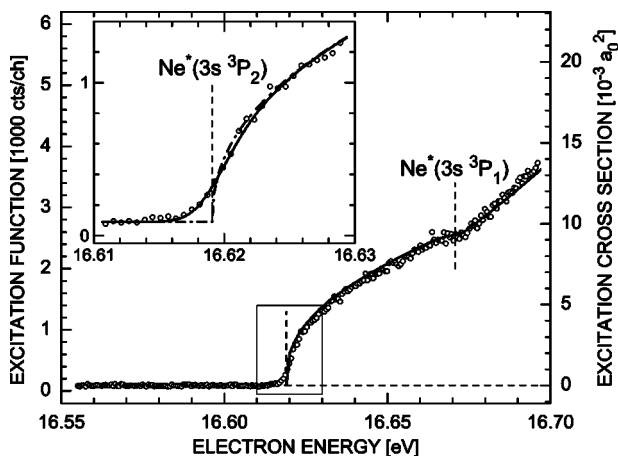


FIG. 6. Threshold measurement of the yield for electron impact excitation of metastable $\text{Ne}^*(3s\ ^3P_2)$ atoms (open circles). The signal below threshold is due to metastable N_2^* molecules (see text). For comparison, the full curve shows the theoretical cross section (in units of $10^{-3}a_0^2$, a_0 is the Bohr radius). Inset: Close-up of the threshold region. The full curve is a fit to the experimental data, resulting from a convolution of the theoretical cross section (chain curve) with a Gaussian resolution function of 4.0 meV.

cah coupling is $\text{Ne}^-(2p^5 3p[5/2]_2 3p)$ [see Table II].

In Table I we compare the energy positions of eight characteristic features with those reported by the Manchester group [5,52,53] and those found in the present *R*-matrix calculation; in most cases, we use the labels given in [5]. Within the respective uncertainties, good mutual agreement is found for the features *B*, *D*, *F*, *G*, and *H*. We do not find the broad resonance reported to lie at 18.350 eV [5,52,53]. Our experimental and theoretical results consistently show a prominent downward cusp at the opening of the $\text{Ne}^*[2p^5(^2P_{3/2})3p\ ^3S_1]$ channel (feature *C*). The sharp peak *I*, previously associated with a threshold resonance at the $\text{Ne}^*(2p^5 3p'[1/2]_0)$ onset [5,52,53], is actually found to be bound by about 10 meV.

For the sharper resonances, we also quote the peak widths (i.e., FWHM; note that these are not fully equivalent to the respective resonance widths in view of their slight asymmetries). Within the respective uncertainties, agreement between the two experimental data sets is found. Our experimental widths agree very well with those predicted theoretically.

In Table II, we present the partial wave composition of the features *A*–*I*, as identified in the theoretical analysis. Below 17 eV six rather broad and overlapping resonances of even parity exist; the three resonances labeled *A* possess a $2p^5 3s[3/2]_2$ core, those denoted *B* have a $2p^5 3s[3/2]_1$ core. The feature *F* is composed of two odd parity resonances with a $2p^5 3p[3/2]_1$ core. The feature *G* consists of three odd parity resonances with $2p^5 3p'[3/2]_1$ core and the peak *H* of two odd parity resonances with $2p^5 3p'[1/2]_1$ core.

B. Scattering cross sections in the range of the $\text{Ne}^-(2p^5 3s^2\ ^2P_{3/2}, ^2P_{1/2})$ resonances

The principal goal of the present work was an improved investigation of the low-lying, very narrow Feshbach resonances $\text{Ne}^-(2p^5 3s^2\ ^2P_{3/2}, ^2P_{1/2})$. They correspond to bound states relative to the two metastable levels, as formed by attaching another spin-paired $3s$ electron to the respective metastable state. The corresponding binding energy is close to 0.5 eV [5], and thus the resonances show up as sharp features in the scattering cross sections around 16.12 and 16.22 eV. In the present work, the absolute energy scale was calibrated with reference to the onset for production of metastable $\text{Ne}^*(3s\ ^3P_2)$ atoms, located at 16.619 075(6) eV (see Sec. III C). Typically, the energy ranges 16.10–16.25 eV (resonance region) and 16.55–16.70 eV (onset for metastable atom production) were covered in each energy scan with energy intervals of about 0.6 meV per channel. Depending on the respective energy drifts, as diagnosed from the apparent position of the $\text{Ne}^-(2p^5 3s^2\ ^2P_{3/2})$ resonance, five to ten scans were summed (accumulation time of one second per channel), and energy drifts between these summed scans were compensated by applying appropriate shifts on the respective relative energy scale (passive spectrum stabilization).

In Fig. 6 we present the result of 560 summed scans around the metastable onset (measurement time 56 seconds per channel). Below the $\text{Ne}^*(3s\ ^3P_2)$ threshold a weak constant signal is observed which is due to the detection of

TABLE I. Peak positions E_p and apparent widths for resonances in e -Ne collisions at incident energies between 16.9 and 19.0 eV. Some of the features labeled by capital letters are the result of overlapping individual resonances (see Table II).

	Classification ^a	Energy ^a (eV)	Width ^a (meV)	Energy ^b (eV)	Width ^b (meV)	Energy ^c (eV)	Width ^c (meV)
B	$2p^5(^2P_{3/2,1/2})3s3p(^3P)$	16.906(10)	117	16.903(3)	113	16.901	117
	$2p^5(^2P_{3/2,1/2})3s3p(^1P)$	18.350(100)					
C	$[2p^5(^2P_{3/2})3p^3S_1] + \epsilon s^d$			18.380(6)		18.382	
D	$2p^5(^2P_{3/2,1/2})3p^2(^1D)$	18.464(15)		18.461(15) ^e		18.447 ^f	
E				18.527(2)	<5	18.527	0.84
F	$2p^5(^2P_{3/2})3p^2(^1S)$	18.580(10)	30	18.573(3)	31(3)	18.570	30
G	$2p^5(^2P_{3/2,1/2})3p^2(^1D)$	18.626(15)	25	18.615(3)	18(4)	18.614	15
H	$2p^5(^2P_{1/2})^3P^2(^1S)$	18.672(10)	50	18.662(3)	42(3)	18.659	38
I	$2p^53p'[1/2]_0 + \epsilon s^g$	18.965(10)	22	18.957(3)	21(4)	18.956	16

^aFrom Table IX in [5] (except for feature C); see also [52,53] for further details.

^bPresent experiment: energy scale calibrated relative to the $\text{Ne}^*(3s^3P_2)$ excitation threshold; the energy positions and widths are evaluated by inspection and/or by appropriate peak fitting procedures (see text).

^cPresent theory: apparent energies and widths of the calculated sum cross section (not convoluted with the experimental resolution function), evaluated by inspection and/or by appropriate peak fitting procedures (see text).

^dCusp structure due to channel opening of the indicated target state; the spectroscopic energy of this level is 18.381 62 eV [47–49].

^eIncreased error bar due to poor statistics.

^fLocal maximum which in a time-delay analysis could not be identified as a resonance.

^gIdentification as threshold resonance, associated with the $\text{Ne}^*(2p^53p'[1/2]_0)$ onset at 18.965 96 eV [47–49]; present work proves that this resonance lies below the indicated onset.

TABLE II. Partial wave resolved theoretical positions and widths for resonances in e -Ne collisions at incident energies between 16.9 and 19.0 eV. The overlap of the individual resonances, labeled by capital letters below, produces the correspondingly labeled features in Table I and in Fig. 5.

Feature	Total J^π	Energy (eV)	Width (meV)	Dominant component
A	$5/2^e$	16.713	152	$(3s[3/2]_2)3p$
A	$1/2^e$	16.755	133	$(3s[3/2]_2)3p$
A	$3/2^e$	16.759	81	$(3s[3/2]_2)3p$
B	$1/2^e$	16.869	225	$(3s[3/2]_1)3p$
B	$5/2^e$	16.884	100	$(3s[3/2]_1)3p$
B	$3/2^e$	16.895	117	$(3s[3/2]_1)3p$
E	$3/2^o$	18.527	0.84	$(3p[5/2]_2)3p$
F	$1/2^o$	18.567	20.1	$(3p[3/2]_1)3p$
F	$3/2^o$	18.579	21.4	$(3p[3/2]_1)3p$
G	$5/2^o$	18.609	9.4	$(3p'[3/2]_1)3p$
G	$3/2^o$	18.612	12.9	$(3p'[3/2]_1)3p$
G	$1/2^o$	18.618	13.2	$(3p'[3/2]_1)3p$
H	$1/2^o$	18.642	26.4	$(3p'[1/2]_1)3p$
H	$3/2^o$	18.659	28.1	$(3p'[1/2]_1)3p$
I	$1/2^e$	18.955	19.4	$(3p'[1/2]_0)4s$

metastable N_2^* molecules; as a result of the gas recycling process the neon gas became somewhat contaminated by nitrogen. As expected, test measurements without gas recycling showed no background. Above the $\text{Ne}^*(3s^3P_2)$ threshold, the background-corrected data are compared with the calculated Ne^* excitation function. The (additional) rise of the metastable atom yield above 16.671 eV [onset of the short-lived $\text{Ne}^*(3s^3P_1)$ level] is due to a rather substantial channel interaction and nicely borne out in both the experimental and theoretical data (note that the 74.4 nm XUV photons, emitted into the full solid angle upon decay of the $\text{Ne}^*(3s^3P_1)$ level, have only a very low probability for being sampled by the metastable atom detector, and thus the contribution of this excitation channel to the metastable atom signal is negligible).

The experimental energy scale is precisely calibrated (to within ± 0.3 meV) by fitting the measured, background corrected data points with the theoretical cross section (onset positioned at the spectroscopic threshold, chain curve in the inset in Fig. 6) and accounting for the finite energy resolution by convolution with a Gaussian function of adjustable width, yielding the full curve in the inset in Fig. 6. At the same time a realistic estimate of the overall energy resolution is obtained; for the measurement shown in Fig. 6 it amounted to 4.0(4) meV (FWHM).

In Fig. 7 we present the resonance profiles (open circles, background subtracted), simultaneously measured for the five scattering angles 22.5° , 45° , 90° , 112.5° , and 135° under the resolution conditions of the data in Fig. 6. We note that the background level (which is only a substantial correction

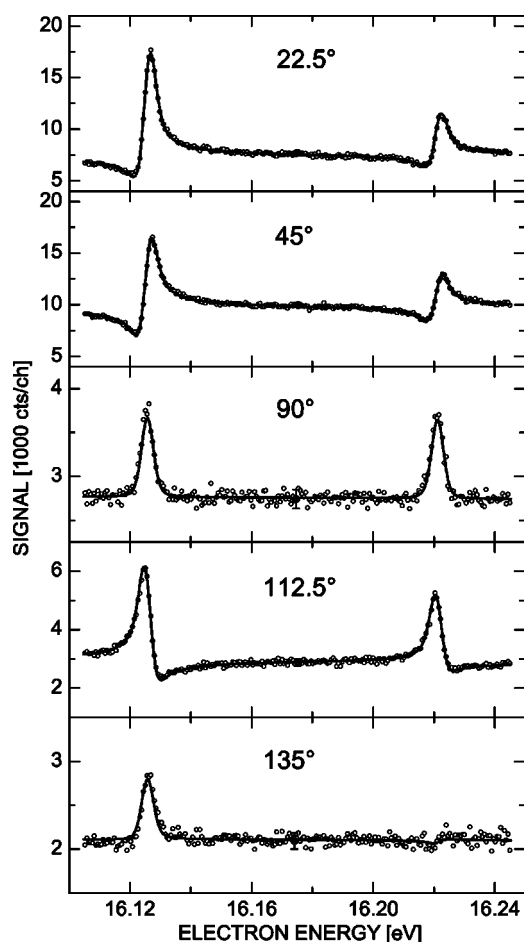


FIG. 7. Profiles for the $\text{Ne}^-(2p^5 3s^2 P_{3/2,1/2})$ resonances, as simultaneously measured at the five scattering angles 22.5° , 45° , 90° , 112.5° , and 135° (open circles, respective average background of 4475/580/41/101/153 counts per channel subtracted). The full curves show fitted resonance profiles involving (consistently at the five angles) a Gaussian resolution function with 4.0 meV FWHM and natural widths of $\Gamma = 1.29$ meV for both resonances with a fine structure separation of 95.5 meV (for details see text). The phase shifts δ_L ($L=0-2$) were also subject of the fitting procedure with resulting values listed in Table III.

at 22.5°) is mainly due (at least at 22.5° and 45°) to electron scattering from surfaces, e.g., from the terminating aperture (diameter 5 mm) of the lens system. The background level depends on the (common) value of the retarding potential in front of the electron detectors. Due to differences in contact potentials, the effective retarding potential may differ for the five detectors. Both the background level and the true scattering intensity are influenced by this effect. Moreover, the detected signals depend on the overall transmission of the two grids (forming the retarding field) and on the detection efficiency of the channel electron multipliers which are not exactly known. Therefore, the background-corrected intensities do not directly reflect the angular dependent scattering cross sections. The full lines in Fig. 7 represent the results of *simultaneous* least squares fits of theoretical cross sections to the data points, using the partial wave formulas (1)–(3) and (5) presented in Sec. II, optimized scattering phase shifts for $L=0, 1, 2$, and phase shifts for the two resonances according

to Eq. (4). The calculated cross sections were convoluted with a Gaussian function of adjustable width to simulate the overall energy resolution. The finite angular resolution (see Sec. III) was neglected. Tests showed that the widths of the two resonances were identical to within 0.1 meV, and we thus assumed in most of the fit calculations that the two resonances have identical widths. The nonidentical efficiencies of the five detectors (see above) were accounted for by appropriate response factors.

Excellent overall agreement between the measured data and the fitted theoretical curves is observed. The agreement at 22.5° is quite remarkable in view of the significant background subtracted at this angle; it demonstrates that the background subtraction procedure is well founded.

An important aspect of the fitting procedure is the choice of the elastic scattering phase shifts [27–29,54–64]. Only the phase shifts for $L=0, 1, 2$ need closer inspection; for $L \geq 3$, Eq. (5) is sufficiently accurate [27–29,55,58,59]. Previously measured and calculated phase shifts are summarized in Table III. The average values of the listed previous phase shifts [27–29,54–64] are $-1.045(30)$, $-0.354(20)$, and $0.157(15)$ rad for the $L=0, 1, 2$ phase shifts (modulo multiples of π), respectively; the numbers in the brackets indicate the scatter of the reported values with respect to the last two given digits. In order to judge the influence of the phase shifts on the fitted values of the resonance parameters, we carried out fit calculations with all the combinations for the $L=0, 1, 2$ phase shifts listed in Table III. Note that the simultaneously fitted detector responses may partially compensate differences in the angle dependent cross sections which arise from small differences between the phase shifts. In all cases an excellent or a good overall fit to the experimental data was obtained. Remaining deviations were most noticeable at 90° , 112.5° , and 135° . In the fit shown in Fig. 7 we allowed for an optimization of the $L=0, 1, 2$ phase shifts and thus obtained our values listed in Table III. We note that with regard to the ratios between the resonance and background scattering signals, variations of the s -wave and d -wave phase shift by ± 0.02 rad (around the average values quoted above) have a clear effect only on the 135° data while variations of the p -wave phase shift by the same amount are mainly visible at 112.5° .

From the fitted angle-dependent resonance profiles (i.e. those in Fig. 7 and those obtained in two further extended data runs at energy widths of 5.6 and 5.8 meV), accurate values for the resonance energies E_r , for the fine structure separation Δ_{fs} and for the natural widths Γ of the resonances were determined; they are listed in Tables IV and V where they are compared with previous experimental and theoretical values [5,28,29,66–76]. We note that the choice of the phase shifts is not the decisive source of uncertainty for our experimental values of the resonance energies and the fine-structure separation. While good agreement is found among the fine-structure separations, the previously recommended resonance energies [5,73] deviate from our values to an extent larger than the combined experimental uncertainties. We cannot offer an explanation for this discrepancy. We note that Brunt *et al.* [73] used two different methods to determine the resonance energies: (i) a simultaneous recording of the Ne^- resonances and of the spectrum for excitation of metastable

TABLE III. Background phase shifts δ_L (rad) ($L=0,1,2,3$) for elastic e -Ne scattering at the electron energy 16.16 eV. Experimental and theoretical results are marked by E and T, respectively. Most of the listed values were obtained by interpolation of phase shifts quoted at neighboring energies.

	δ_0	δ_1	δ_2	δ_3	
Thompson [27]	-1.040	-0.335	0.162	0.035	T
Andrick [28]	-1.042	-0.358	0.162	0.031	E
Williams [54]	-1.035(17)	-0.351(10)	0.150(12)		E
Fon and Berrington [55]	-1.063	-0.343	0.179	0.031	T
Brewer <i>et al.</i> [56]	-1.02	-0.36	0.16	0.03	E
Peach [57] ^a	-1.058	-0.349	0.142		T
McEachran and Stauffer [58]	-1.056	-0.361	0.156	0.033	T
Register and Trajmar [59]	-1.031(30)	-0.347(24)	0.149(15)	0.030(5)	E
Dasgupta and Bhatia [60]	-1.057	-0.364	0.139	0.036	T
Nakanishi and Schrader [61]	-1.075	-0.358	0.152	0.039	T
Saha [62]	-1.026	-0.339	0.151	0.032	T
Dubé <i>et al.</i> [29]	-1.027	-0.349	0.175		E
Kerner [63]	-1.052	-0.369	0.162		T
Elkilany [64]	-1.041	-0.370	0.163		T
Heindorff <i>et al.</i> [65] ^b	-1.043	-0.325	0.164		E
Present experiment	-1.061	-0.357	0.165		E
Present theory	-1.051	-0.363	0.151	0.031	T

^aValues obtained with model potential.

^bPresent least squares fit to the angular distribution measured 0.24 eV above the $\text{Ne}^-(^2P_{3/2})$ resonance (Fig. 2 in [65]), using Born phase shifts for $L \geq 3$.

$\text{Ne}^*(3s\ ^3P_2)$ atoms; (ii) measuring—with a mixture of the gases helium and neon as the target—the energies of features in neon elastic scattering and metastable excitation spectra with respect to the energy of the $\text{He}^-(^2S_{1/2})$ resonance, then placed at 19.366(5) eV [73] (this value agrees with the recent accurate value of 19.365(1) eV [22]). The two ap-

proaches gave apparent energies which differed by 8 meV, the latter giving the higher energy. The quoted Ne^- resonance energies reflect a weighted mean of the two energy scales obtained with the methods (i) and (ii) [73].

The resonance positions predicted by the present BSRM theory are approximately 22.3 and 18.8 meV above the ex-

TABLE IV. Resonance energies E_r and fine-structure separation ΔE_{fs} of the $\text{Ne}^-(2p^5 3s^2\ ^2P_{3/2,1/2})$ Feshbach resonances. Experimental and theoretical results are marked by E and T, respectively.

	E_r [eV]		ΔE_{fs} (meV)	
	$^2P_{3/2}$	$^2P_{1/2}$		
Simpson and Fano [66]		16.0(1) ^a	100(20)	E
Kuyatt <i>et al.</i> [67]	16.040(20)	16.135(20)	95(2)	E
Andrick and Ehrhardt [68]			95	E
Weiss and Krauss [69]		16.17 ^b		T
Sanche and Schulz [70]	16.10–16.12(3)	16.19–16.22(3)	95(2)	E
Kisker [71]	16.12(2)			E
Roy <i>et al.</i> [72]			95	E
Brunt <i>et al.</i> [73]	16.111(8)	16.208	97(1)	E
Noro <i>et al.</i> [74]		16.182 ^b		T
Clark [75]		16.161 ^b		T
Present experiment	16.1257(10)	16.2212(10)	95.5(3)	E
Present theory	16.148	16.240	92	T

^aMean position of the feature.

^bPosition of the 2P resonance in a nonrelativistic model.

TABLE V. Resonance widths Γ of the $\text{Ne}^-(2p^5 3s^2 {}^2P_{3/2,1/2})$ Feshbach resonances. If not noted otherwise, the widths of the two resonances are identical within the respective uncertainty. Experimental and theoretical results are marked by E and T, respectively.

	Width Γ (meV)	
Simpson and Fano [66]	>1	E
Ehrhardt <i>et al.</i> [76]; Andrick [28]	1.4	E
Roy <i>et al.</i> [72]	1.4–1.8	E
Brunt <i>et al.</i> [73]	1.3(4)	E
Noro <i>et al.</i> [74]	0.9	T
Dubé <i>et al.</i> [29]	1.30(15)	E
Clark (cited in [5])	3	T
Present experiment	1.27(7)	E
Present theory	$1.52 ({}^2P_{3/2}), 1.53 ({}^2P_{1/2})$	T

perimental results, and hence the theoretical fine-structure splitting of 92.0 meV is 3.5 meV too small. Nevertheless, we judge the agreement between experiment and theory as very satisfactory.

In addition, we derive accurate resonance widths from the combined fits to the experimental data in Fig. 7; the resulting values and previous results are summarized in Table V. Note that the fitting procedure yields *both* the effective experimental resolution and the intrinsic resonance widths Γ . The fitted resolution 4.0(1) meV agrees with that determined from the appearance of the onset for metastable atom production (Fig. 6) and was consistently obtained in all the fits using the various phase shift combinations listed in Table III. As is well known, variations of the experimental resolution on the one hand and of the resonance width on the other hand influence the measured resonance profiles rather differently (see [28,29,73] for a detailed discussion). In the present case, where the background scattering cross section is well known, reliable values for the natural width Γ may be obtained even for experimental energy widths much larger than Γ [28,29,73], as long as the resolution function is well characterized and the statistical quality of the data sufficiently good. It is thus not astounding (but still satisfactory) that the widths derived in [28,29,73] at resolution levels between about 20 and 50 meV agree very well with the value determined in the present work. The error bar for our width mainly reflects the variation of the fitted widths when different sets of phase shifts are used. The quoted value is the average over the different fits.

The theoretical width of the two resonances is very similar (1.52 and 1.53 meV, respectively), but 20% larger than what we found experimentally. Nevertheless, this is a major improvement over previous calculations of the resonance width by Noro *et al.* [74], who obtained 0.9 meV in a 17-state nonrelativistic *R*-matrix model, and by Clark and Taylor who, according to Buckman and Clark [5], obtained 3 meV.

Finally, we compare our fitted differential cross sections as well as the respective angle-integrated cross sections with those calculated in the present work (see Fig. 8). The theoretical cross sections, calculated with the help of the program MJK of Grum-Grzhimailo [77], were convoluted with a

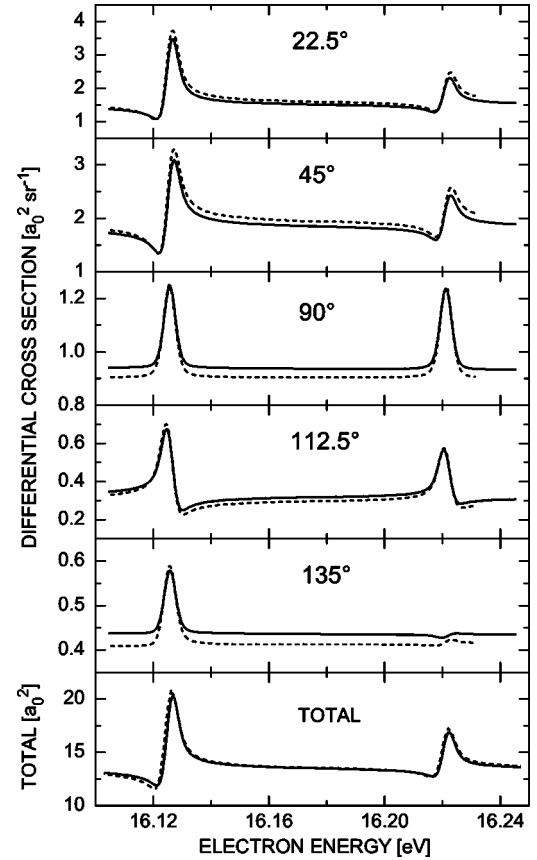


FIG. 8. Comparison of the differential cross sections (in units of $a_0^2 \text{sr}^{-1}$, a_0 is the Bohr radius) for electron scattering from neon atoms in the energy range of the $\text{Ne}^-(2p^5 3s^2 {}^2P_{3/2,1/2})$ Feshbach resonances, as obtained (i) from the fits to our experimental data (full curves) and (ii) in the BSRM calculation (broken curves, resonances shifted by -22.3 meV for ${}^2P_{3/2}$ and -18.8 meV for ${}^2P_{1/2}$). The bottom graph illustrates the angle-integrated cross sections. In all cases the resonance profiles were convoluted with a Gaussian function of 4.0 meV FWHM to simulate experimental conditions.

Gaussian function of 4 meV FWHM to simulate the experimental resolution. In order to allow for a better comparison between the experimental and theoretical shapes of the curves, we shifted and stretched the energy scale in the BSRM calculation to give the correct positions and fine-structure splitting of the two resonances. As seen from Table IV, the corresponding shifts were -22.3 meV for the ${}^2P_{3/2}$ and -18.8 meV for the ${}^2P_{1/2}$ resonance. A large part of the differences between the two cross section sets can be traced to the fact that the respective resonance widths differ by 20%. Moreover, the background cross sections differ in an angle-dependent way, reflecting the fact that the theoretical background phase shifts slightly deviate from our fitted phase shifts for $L=0-2$.

V. CONCLUSIONS

Using an experimental setup, which combines a laser photoelectron source with a dense supersonic beam target, we have studied elastic and inelastic electron scattering from

neon atoms in the energy range 16–19 eV with an experimental energy resolution of about 4 meV. Improved values for the energy positions, the widths, and the fine structure separation of the low-lying $\text{Ne}^-(2p^5 3s^2 {}^2P_{3/2,1/2})$ Feshbach resonances have been determined from detailed fits of resonant scattering calculations to the experimental data. Moreover, the excitation function for production of the metastable $\text{Ne}^*(3s {}^3P_2, {}^3P_0)$ levels has been measured with a resolution of 4–6 meV. The experimental results are compared with improved *R*-matrix calculations which provide an excellent overall description of the measured data. The existence of a very narrow Feshbach resonance, predicted to be located 49 meV below the $\text{Ne}^*(2p^5 3p [5/2]_2)$ level, was experimentally confirmed. In a forthcoming paper, we shall present results for the low-lying Feshbach resonances in argon, as obtained at overall resolutions between 4 and 6 meV.

ACKNOWLEDGMENTS

This work has been supported by the Deutsche Forschungsgemeinschaft through Forschergruppe FOR 307 (Niederenergetische Elektronenstreuprozesse), by the Forschungszentrum Lasermesstechnik und Diagnostik, and by the Forschungszentrum Optische Technologien und laser-gesteuerte Prozesse. We gratefully acknowledge the mechanical workshop of Universität Kaiserslautern for their remarkable achievement in the realization of the new apparatus. We thank S. Götte, E. Leber, and A. Landwehr for experimental support in the early stages of this experiment and K. Zinsmeister for technical support. We acknowledge C. Kerner and W. Meyer for communicating their elastic background phase shifts. Two of us (O.Z. and K.B.) acknowledge support from the National Science Foundation under Grant Nos. PHY-0244470 and PHY-0311161.

-
- [1] G. J. Schulz, *Rev. Mod. Phys.* **45**, 378 (1973); **45**, 423 (1973).
 - [2] *Applied Atomic Collision Physics*, edited by H. S. W. Massey and D. R. Bates (Academic, New York, 1982), Vol. 1.
 - [3] *Electron-molecule Collisions*, edited by I. Shimamura and K. Takayanagi (Plenum, New York, 1984).
 - [4] *Electron-molecule Interactions and Their Applications*, edited by L. G. Christophorou (Academic, New York, 1984), Vols. I and II.
 - [5] S. J. Buckman and C. W. Clark, *Rev. Mod. Phys.* **66**, 539 (1994).
 - [6] A. Zecca, G. P. Karwasz, and R. S. Brusa, *Riv. Nuovo Cimento* **19**, 1 (1995).
 - [7] L. G. Christophorou and J. K. Olthoff, *Adv. At., Mol., Opt. Phys.* **44**, 59 (2000).
 - [8] M. J. Brunger and S. J. Buckman, *Phys. Rep.* **357**, 215 (2002).
 - [9] H. Hotop, M.-W. Ruf, M. Allan, and I. I. Fabrikant, *Adv. At., Mol., Opt. Phys.* **49**, 85 (2003).
 - [10] K. P. Rohr and F. Linder, *J. Phys. B* **9**, 2521 (1976).
 - [11] K. Jung, Th. Antoni, R. Müller, K. H. Kochem, and H. Ehrhardt, *J. Phys. B* **15**, 3535 (1982).
 - [12] F. H. Read, *Phys. Scr.* **27**, 103 (1983).
 - [13] M. Allan, *J. Phys. B* **28**, 5163 (1995).
 - [14] M. Allan, *Phys. Rev. Lett.* **87**, 033201 (2001).
 - [15] A. Chutjian, A. Garscadden, and J. M. Wadehra, *Phys. Rep.* **264**, 393 (1996).
 - [16] D. Field, G. Mrozek, D. W. Knight, S. Lunt, and J. P. Ziesel, *J. Phys. B* **21**, 171 (1988).
 - [17] D. Field, D. W. Knight, G. Mrozek, J. Randell, S. L. Lunt, J. B. Ozenne, and J. P. Ziesel, *Meas. Sci. Technol.* **2**, 757 (1991).
 - [18] D. Field, S. L. Lunt, and J. P. Ziesel, *Acc. Chem. Res.* **34**, 291 (2001).
 - [19] S. V. Hoffmann, S. L. Lunt, N. C. Jones, D. Field, and J.-P. Ziesel, *Rev. Sci. Instrum.* **73**, 4157 (2002).
 - [20] R. J. van Brunt and A. C. Gallagher, in *Electronic and Atomic Collisions*, edited by G. Watel (North-Holland, Amsterdam, 1978), p. 129 ff.
 - [21] R. E. Kennerly, R. J. van Brunt, and A. Gallagher, *Phys. Rev. A* **23**, 2430 (1981).
 - [22] A. Gopalan, J. Bömmels, S. Götte, A. Landwehr, K. Franz, M.-W. Ruf, H. Hotop, and K. Bartschat, *Eur. Phys. J. D* **22**, 17 (2003).
 - [23] P. Hammond, *J. Phys. B* **29**, L231 (1996).
 - [24] J. Comer and F. H. Read, *J. Phys. B* **4**, 1055 (1971).
 - [25] N. F. Mott and H. S. W. Massey, *The Theory of Atomic Collisions* (Oxford University Press, Oxford, 1965).
 - [26] S. Flügge, *Lehrbuch der Theoretischen Physik IV* (Springer-Verlag, Berlin, 1964).
 - [27] D. G. Thompson, *J. Phys. B* **4**, 468 (1971).
 - [28] D. Andrick, *Adv. At. Mol. Phys.* **9**, 271 (1973).
 - [29] D. Dubé, D. Tremblay, and D. Roy, *Phys. Rev. A* **47**, 2893 (1993).
 - [30] T. Miller and B. Bederson, *Adv. At. Mol. Phys.* **13**, 1 (1978).
 - [31] D. G. Thompson, *Proc. R. Soc. London, Ser. A* **294**, 160 (1966).
 - [32] O. Zatsarinny and K. Bartschat, *J. Phys. B* **37**, 2173 (2004).
 - [33] V. Zeman and K. Bartschat, *J. Phys. B* **30**, 4609 (1997).
 - [34] K. A. Berrington, W. B. Eissner, and P. H. Norrington, *Comput. Phys. Commun.* **92**, 290 (1995).
 - [35] K. Bartschat, E. T. Hudson, M. P. Scott, P. G. Burke, and V. M. Burke, *J. Phys. B* **29**, 115 (1995).
 - [36] T. W. Gorczyca and N. R. Badnell, *J. Phys. B* **30**, 3897 (1997).
 - [37] K. Bartschat, *Comput. Phys. Commun.* **114**, 168 (1998).
 - [38] C. P. Ballance and D. C. Griffin, *J. Phys. B* **37**, 2943 (2004).
 - [39] D. C. Griffin (private communication).
 - [40] R. Campargue, *J. Phys. Chem.* **88**, 4466 (1984).
 - [41] S. Götte, A. Gopalan, J. Bömmels, M.-W. Ruf, and H. Hotop, *Rev. Sci. Instrum.* **71**, 4070 (2000).
 - [42] J. Bömmels, dissertation, Univ. Kaiserslautern, 2003 (unpublished).
 - [43] J. M. Weber, M.-W. Ruf, and H. Hotop, *Eur. Phys. J. D* **7**, 587 (1999).
 - [44] I. D. Petrov, V. L. Sukhorukov, E. Leber, and H. Hotop, *Eur. Phys. J. D* **10**, 53 (2000).
 - [45] A. Gopalan, E. Leber, J. Bömmels, S. P. H. Paul, M. Allegrini, M.-W. Ruf, and H. Hotop, *Eur. Phys. J. D* **30**, 163 (2004).
 - [46] J. Bömmels, E. Leber, A. Gopalan, J.-M. Weber, S. Barsotti,

- M.-W. Ruf, and H. Hotop, *Rev. Sci. Instrum.* **72**, 4098 (2001).
- [47] V. Kaufman and L. Minnhagen, *J. Opt. Soc. Am.* **62**, 92 (1972).
- [48] K. S. E. Eikema, W. Ubachs, and W. Hogervorst, *Phys. Rev. A* **49**, 803 (1994).
- [49] P. J. Mohr and B. N. Taylor, *J. Phys. Chem. Ref. Data* **28**, 1713 (1999).
- [50] E. P. Wigner, *Phys. Rev.* **73**, 1002 (1948).
- [51] P. Frey, M. Lawen, F. Breyer, H. Klar, and H. Hotop, *Z. Phys. A* **304**, 155 (1982).
- [52] J. N. H. Brunt, G. C. King, and F. H. Read, *J. Phys. B* **9**, 2195 (1976).
- [53] S. J. Buckman, P. Hammond, G. C. King, and F. H. Read, *J. Phys. B* **16**, 4219 (1983).
- [54] J. F. Williams, *J. Phys. B* **12**, 265 (1979).
- [55] W. C. Fon and K. A. Berrington, *J. Phys. B* **14**, 323 (1981).
- [56] D. F. C. Brewer, W. R. Newell, S. F. W. Harper, and A. C. H. Smith, *J. Phys. B* **14**, L749 (1981).
- [57] G. Peach, *Comments At. Mol. Phys.* **11**, 101 (1982).
- [58] R. P. McEachran and A. D. Stauffer, *J. Phys. B* **16**, 4023 (1983).
- [59] D. F. Register and S. Trajmar, *Phys. Rev. A* **29**, 1785 (1984).
- [60] A. Dasgupta and A. K. Bhatia, *Phys. Rev. A* **30**, 1241 (1984).
- [61] H. Nakanishi and D. M. Schrader, *Phys. Rev. A* **34**, 1823 (1986).
- [62] H. P. Saha, *Phys. Rev. A* **39**, 5048 (1989).
- [63] C. Kerner, dissertation, Univ. Kaiserslautern, 1995 (unpublished).
- [64] S. A. Elkilany, *Nuovo Cimento D* **19**, 1525 (1997).
- [65] T. Heindorff, J. Höfft, and E. Reichert, *J. Phys. B* **6**, 477 (1973).
- [66] J. A. Simpson and U. Fano, *Phys. Rev. Lett.* **11**, 158 (1963).
- [67] C. E. Kuyatt, J. A. Simpson, and S. R. Mielczarek, *Phys. Rev.* **138**, A385 (1965).
- [68] D. Andrick and H. Ehrhardt, *Z. Phys.* **192**, 99 (1966).
- [69] A. Weiss and M. Krauss, *J. Chem. Phys.* **52**, 4363 (1970).
- [70] L. Sanche and G. J. Schulz, *Phys. Rev. A* **5**, 1672 (1972).
- [71] E. Kisker, *Phys. Lett.* **41A**, 173 (1972).
- [72] D. Roy, A. Delâge, and J.-D. Carette, *J. Phys. E* **8**, 109 (1975).
- [73] J. N. H. Brunt, G. C. King, and F. H. Read, *J. Phys. B* **10**, 1289 (1977).
- [74] T. Noro, F. Sasaki, and H. Tatewaki, *J. Phys. B* **12**, 2217 (1979).
- [75] C. W. Clark, in *Advances in Laser Physics I*, edited by W. C. Stwalley and M. Lapp, AIP Conf. Proc., No. 146 (AIP, New York, 1986).
- [76] H. Ehrhardt, L. Langhans, F. Linder, and H. S. Taylor, *Phys. Rev.* **173**, 222 (1968).
- [77] A. N. Grum-Grzhimailo, *Comput. Phys. Commun.* **152**, 101 (2003).